Sensors & Actuators: B. Chemical 370 (2022) 132398

Contents lists available at ScienceDirect

Sensors and Actuators: B. Chemical

journal homepage: www.elsevier.com/locate/snb

Ppb-level NO_2 sensing properties at room temperature of ultra-thin SnS_2 nanopetals annealed at different temperatures

Yueyue Li [a], Meng Dai [a], Jihao Bai [a], Yilin Wang [a], Yuan Li [a], Chenchang Wang [a], Fengmin Liu [a,*], Peng Sun [a,b], Tianshuang Wang [a], Geyu Lu [a,b,**]

[a] State Key Laboratory of Integrated Optoelectronics, Key Laboratory of Advanced Gas Sensor, Jilin Province, College of Electronic Science and Engineering, Jilin University, Changchun 130012, China

[b] International Center of Future Science, Jilin University, Changchun 130012, China

ARTICLE INFO

Keywords:
Ultra-thin SnS_2 nanopetals
NO_2 sensors
Low detection limit
Sulfur vacancies
Room temperature

ABSTRACT

Two-dimensional SnS_2 with stable electron transport capacity, high specific surface area, and high surface activity due to defects such as sulfur vacancies, is a suitable candidate for gas sensors at room temperature. Here, ultra-thin SnS_2 nanopetals are synthesized and planar type sensors are obtained through coating SnS_2 on a substrate with interdigitated electrodes. Samples annealed at different temperatures were characterized and their gas-sensing properties were compared. The sensor annealed at 200 °C in the air of the muffle furnace (SnS_2-200) exhibits the best sensing performance with the high response of 24.20 to 100 ppb NO_2 at RT and ultra-low detection limit of 5 ppb NO_2. Moreover, the SnS_2-200 sensor also possesses good repeatability, selectivity and long-term stability. The excellent sensing performances prove that the SnS_2 holds excellent application prospects in the detection of trace-level NO_2.

1. Introduction

The trace-level nitrogen oxides (NO_x) come from a wide range of sources, such as natural gas burning, smoking, and heating supply systems [1,2]. The secure standard of NO_2 is set to 21.25 ppb by the World Health Organization (WHO) [3]. Recent researches show that long-term exposure to NO_2 even at low concentration increases the risk of cardiovascular diseases, and especially respiratory diseases in humans [4,5]. Therefore, it is essential to develop portable gas sensors with a low detection limit (LOD) to meet the requirement for trace-level NO_2 detection.

Gas sensors based on metal oxides semiconductors have gained widespread attentions due to the advantages of simple structure, high portability, low cost, and low power consumption [6,7]. Recently researchers have found that the sulfur vacancies (S_v) in metal sulfide semiconductors also have a strong adsorption capacity for NO_2, which makes the sensors based on sulfide more suitable for detecting NO_2 regardless of the presence of oxygen in the environment [8,9]. On the other hand, two-dimensional (2D) material holds great potential as the candidate for gas sensors due to its unique geometry, large surface area and quantum size effect. Tin sulfide (SnS_2) is a common 2D material [8,10] with excellent properties including high specific surface area, tunable layer-dependent electronic properties, and surface affinity that are beneficial for surface reaction in gas sensing process [11,12].

There have been some studies on the application of SnS_2 in gas sensors at room temperature (RT). Gu et al. fabricated the sensors based on disorderly stacked SnS_2 nanosheets to detect ppm-level NO_2 with the green light activation [11]. EOM et al. found that SnS_2 nanoflowers exhibits more stable and excellent gas sensitivity under blue light [6]. However, the LOD of sensors cannot meet the requirements of trace-level NO_2 detection in these works, and additional photoexcitation is required to realize the sensing. Effective strategies are still needed to improve the sensing performance of SnS_2 at RT. It has been demonstrated that the gas-sensing properties of 2D materials increase with the decrease of thickness [13,14], and the surface defect density of SnS_2 controlling by low-temperature annealing also affect the gas-sensing properties [15,16]. Therefore, minimizing the thickness of SnS_2 nanosheets and increasing the content of surface-active sites by

* Corresponding author.
** Corresponding author at : State Key Laboratory of Integrated Optoelectronics, Key Laboratory of Advanced Gas Sensor, Jilin Province, College of Electronic Science and Engineering, Jilin University, Changchun 130012, China.
E-mail addresses: liufm@jlu.edu.cn (F. Liu), lugy@jlu.edu.cn (G. Lu).

https://doi.org/10.1016/j.snb.2022.132398
Received 5 April 2022; Received in revised form 28 June 2022; Accepted 15 July 2022
Available online 18 July 2022

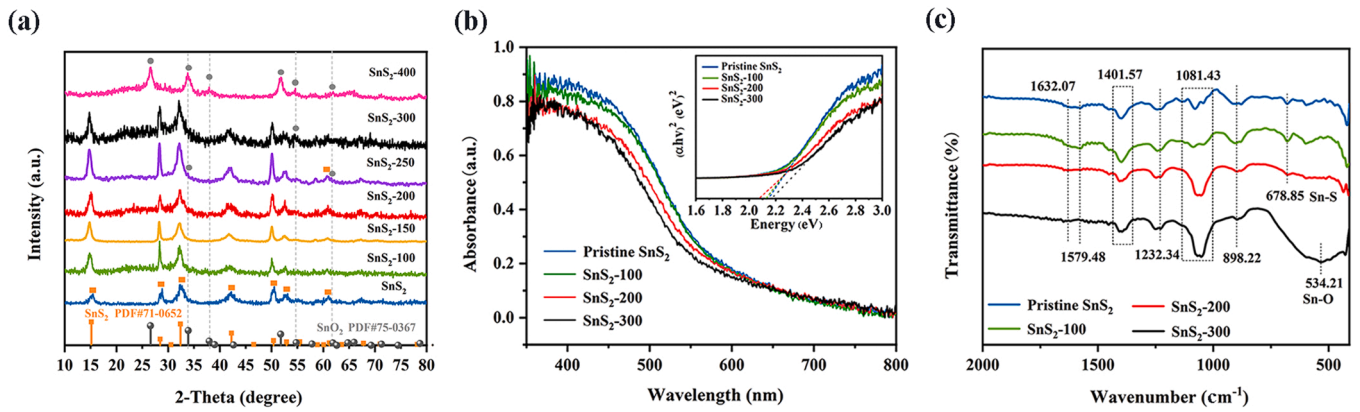

Fig. 1. (a) The XRD patterns of different samples including the PDF file No.71–0652 of SnS_2, and the PDF file No.75–0367 of SnO_2; **(b)** the UV–visible absorption spectra and the optical bandgap (inset) of samples; **(c)** FTIR spectra of samples.

low-temperature annealing are very likely to be effective strategies to improve the sensitivity of SnS_2 to NO_2.

In this work, SnS_2 flowers composed of ultra-thin nanopetals are obtained through the one-step solvothermal method and gas sensors are fabricated by coating SnS_2 on substrates with interdigitated electrodes. The sensitive characteristics of the sensors annealed in the air of the muffle furnace at different temperatures to NO_2 are investigated and discussed. What's more, the properties of sensors are also investigated when exciting by the green light, and the gas-sensing mechanism of the sensors is discussed and analyzed using the adsorption model.

2. Experimental

2.1. The fabrication of gas sensors based on SnS_2 materials

According to the method in ref [17], pristine SnS_2 was obtained by hydrothermal synthesis at 180 °C for 12 h. Pristine SnS_2 were mixed with ethanol to form a slurry and then brushed to the Al_2O_3 substrates (10 mm × 10 mm) with 15 pairs of Au interdigital electrodes, which were shown in Fig. S1. The brushed ceramic substrates were dried in an oven of 60 °C and then annealed in the air of the muffle furnace (YFX7/12Q-GC, SHANGHAI Y-FENG ELECTRICAL FURNACE CO., LTD) at 100 °C, 150 °C, 200 °C, 250 °C, 300 °C, and 400 °C with the heating rate of 10 °C/min for 1 h and the obtained sensors were labeled as SnS_2-100, SnS_2-150, SnS_2-200, SnS_2-250, SnS_2-300, and SnS_2-400, respectively.

2.2. The measurement of gas sensors based on SnS_2 materials

A static method similar to ref [18] was employed to evaluated sensing properties of these sensors. The relative humidity (RH) in the testing room was kept at 50 % ± 10 %, and the temperature was about 25 ± 5 °C. Firstly, the sensor was placed in an air chamber. When the resistance came to be stable in a 1 L air chamber, the sensor will be transferred into another 1 L gas chamber filled with a certain concentration of NO_2, which was prepared by injecting a certain volume of NO_2 standard gas through the injection syringe into the chamber. After the resistance reached high enough and was stable again, the sensor will be returned into the air chamber immediately. The gas response was defined as $S = R_g/R_a$ to the oxidizing gases and $S = R_a/R_g$ to the reducing gases, where R_g and R_a were the stable resistance values in gas chamber and air chamber, respectively. The time of response (t_{res}) or recovery (t_{rec}) could be read from the resistance curve, which was defined as the time that it took to reach 90 % variation of resistance upon exposure to gas and air. In addition, when the sensor was tested under the 520 nm light, LEDs as the light source (purchased from LG Electronics Company in Korea) were installed 1.5 cm right above the sensor. The light intensities of the LEDs were 0.12 mW/cm^2, measured by a light irradiation meter (UV-313/340, Zhuhai Tianchuan Instrument Company, China). The RH values in the two chambers (30 %−90 % RH) were provided by the humidity cabinet with the setting temperature of 25 °C (Shanghai ES PC Environment Equipment Corporation, China). During the process of investigating the effect of humidity on sensor performance, both chambers were placed in the humidity cabinet to keep for ten minutes. After the humidity in chambers was near to the cabinet, NO_2 gas would be injected into one of the chambers and the following test steps are the same as described earlier. In addition, the sensors are heated by the ceramic heating plate. Two leads of the heating plate are connected to the DC power supply, and the working temperature of the sensors can be controlled at 50 °C, 100 °C, and 150 °C by adjusting the voltage of the power supply.

2.3. Characterization of samples

The crystal structures of samples were characterized by a powder X-ray diffractometer (XRD, Rigaku D/Max-2550 VX-ray diffractometer) assembled with Cu Kα radiation (λ = 0.15418 nm and 2θ = 10°−80°). Ultraviolet-visible (UV–vis) diffuse reflectance spectra were performed by a UV–vis spectrophotometer (shimadzu UV-2550, Japan). Fourier transform infrared spectrometer (FTIR) spectrum was tested using a Nicolet iS10 FT-IR spectrometer. Field emission scanning electron microscope (FESEM, JEOL JSM-7500 F, operating at an accelerating voltage of 15 kV) and high-resolution transmission electron microscope (TEM, on a JEOL JSM-2100 F operating at an accelerating voltage of 200 kV) were applied to analyze the morphology and structures. The X-ray photoelectron spectroscopy (XPS) was performed by Thermo Fischer ESCALAB 250Xi to examine the chemical binding energy of the elements. All binding energies were calibrated with the saturated hydrocarbon C 1 s peak at 284.8 eV. The current-voltage (I–V) curves of samples were studied using an electrochemical workstation (CHI611C, Shanghai Instrument Corporation, China).

3. Result and discussion

3.1. The characteristics of samples

The XRD patterns of samples are shown in Fig. 1. The diffraction peaks of Pristine SnS_2, SnS_2-100, SnS_2-150, and SnS_2-200 completely conform to the standard card of hexagonal phase SnS_2 (JCPDS No. 75–0367), and there are no peaks of other phases indicating the purity of the materials. In the pattern of SnS_2-250 and SnS_2-300, several characteristic peaks of SnO_2 weakly appear at 33.87°, 54.75° and 61.88°, which proves that a small amount of SnS_2 have been oxidized at 250 °C and 300 °C. However, the diffraction peaks of SnS_2-400 are accordance

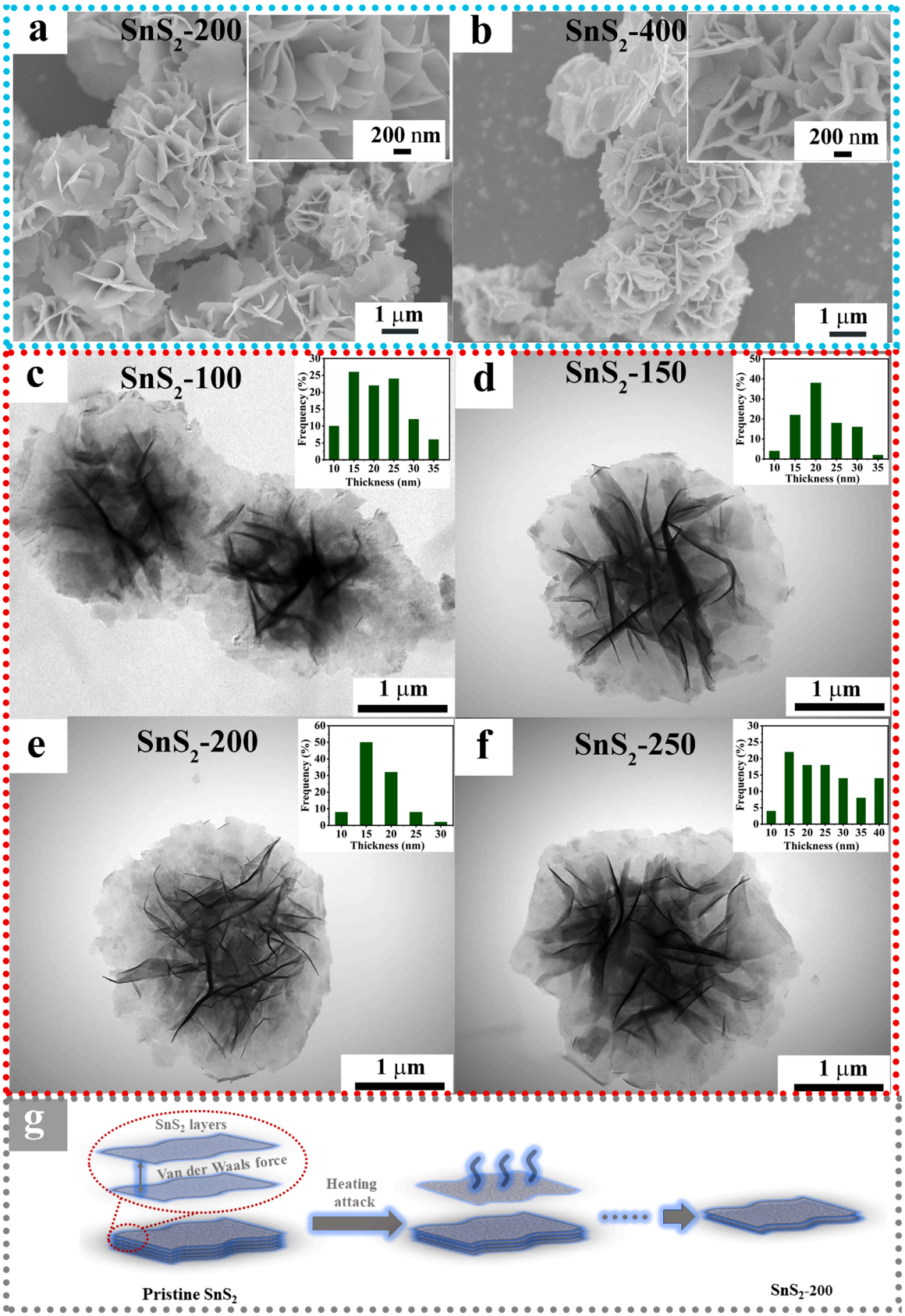

Fig. 2. (a-b) The SEM pictures of SnS_2-200 and SnS_2-400; (c-f) the TEM pictures of SnS_2-100, SnS_2-150, SnS_2-200, and SnS_2-250 (the insets are the thickness distribution of nanosheets in samples, respectively); (g) the diagram of SnS_2 nanosheets thickness change.

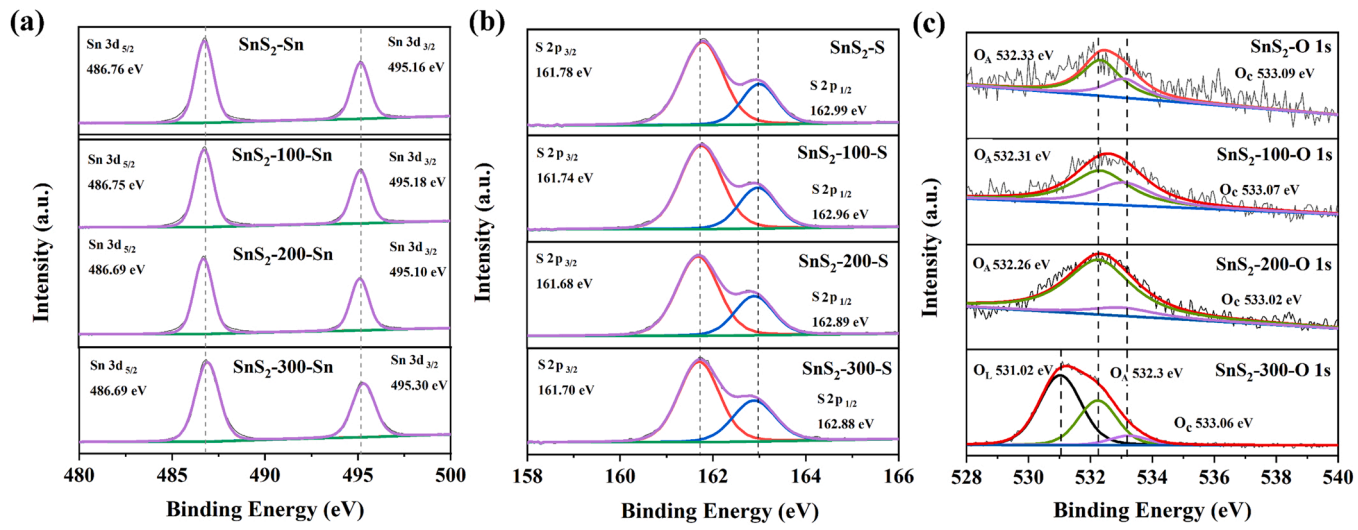

Fig. 3. XPS spectra of samples: **(a)** Sn 3d; **(b)** S 2p; **(c)** O 1s.

with the standard card of SnO_2 (JCPDS card No.71–0652) without characteristic peaks of SnS_2. This result is consistent with the results of TG curve in ref [19], where a significant weight loss occurs from 200 °C to 450 °C, indicating the transition of SnS_2 to the lighter SnO_2 in this temperature range. Therefore, the annealing temperatures in the air of the muffle furnace can be controlled below 200 °C to prevent SnS_2 from being partially oxidized.

SnS_2 is a kind of narrow bandgap semiconductor whose optical bandgap can be obtained by absorption spectra and Tauc plot in Fig. 1 **(b)**. The absorption band edges of samples are at about 560–590 nm. Obviously, E_g varies slightly for the samples annealing at different temperatures which is attributed to the defects levels near to conductive band (CB) in the crystal introduced by defects such as S_v in the samples [20,21]. The E_g of SnS_2-200 is the minimal, may be related to the most S_v it contains.

The FTIR spectra is shown in Fig. 1**(c)**. The peaks appeared at 678.85, and 534.21 cm^{-1} were due to Sn-S and Sn-O bonds, respectively [22]. The appearance of the peaks at ~1232.34 and ~1401.57 cm^{-1} are attributed to the C-OH and C-H stretching vibration, respectively [23, 24]. In addition, the absorption peak at ~1632.07 cm^{-1} is attributed to C═O stretching vibrations of amide, which is derived from raw material of thioacetamide (TAA) and the absorption peak at ~1579.48 cm^{-1} belongs to the stretching vibrations of amine groups (−NH_2) [25,26]. The bands at 1081.43 and 898 cm^{-1} are respectively corresponding to the stretching vibration and bending vibration of C–N bond [23]. By comparisons, with the increase of annealing temperature, the vibration intensity of the amide group on the sample surface gradually decreases, indicating the disappearance of the amide group. The disappearance of this group corresponds to the TG result from 30 °C to 200 °C in ref [27]. Annealing at a proper temperature can not only improve the crystallinity and S_v density of the material to a certain extent, but also effectively control the content of residual functional groups on the surface to improve the stability of the sensors in air.

The SEM and TEM pictures of SnS_2 are shown in Fig. 2(a-f) and Fig. S2. The synthesized SnS_2 presents flower-like structure which are made up of the 2D ultra-thin nanopetals. The formation process of flowers could be analyzed as follows. TAA will hydrolyze with trace water contained in the solution to slowly produce H_2S, which will reacts with Sn^{4+} to generate SnS_2 crystal nuclei [28]. Due to the crystal anisotropy and its intrinsic characteristics, the SnS_2 crystal nucleus will further nucleate in supersaturated salt solution and slowly grow into ultra-thin 2D nanosheets during the process of hydrothermal reaction according to the Gibbs-Thomson law [29,30]. In addition, SnS_2 nanosheets will aggregate and form flower-like structures at the gas-liquid interface using the generated H_2S bubbles with high energy as self-assembly templates for minimizing the interface energy [21].

Table 1
The atomic ratio of elements including Sn, S, and O (O_L, O_A, O_C) in samples.

Samples	Sn (%)	S (%)	Sn: S	O		
				O_L (%)	O_A (%)	O_C (%)
Pristine SnS_2	32.79	64.76	1: 1.97	0	1.89	0.56
SnS_2-100	31.74	62.50	1: 1.97	0	4.34	1.42
SnS_2-200	31.31	60.06	1: 1.92	0	7.15	1.48
SnS_2-300	32.19	37.84	1: 1.18	20.70	8.22	1.05

$$CH_3CSNH_2 + H_2O \rightarrow CH_3CONH_2 + H_2S \quad (1)$$

$$Sn^{4+} + 2H_2S \rightarrow SnS_2 + 4H^+ \quad (2)$$

As shown in the SEM pictures in Fig. 2(a-b) and Fig. S2, the morphology of nanopetals changes faintly with the increase of temperature from 100 °C to 300 °C. However, the surfaces of the nanopetals are no longer smooth until the temperature rises to 400 °C, with many small SnO_2 particles appearing, which is caused by the oxidation of abundant SnS_2 on the surface. As can be seen from the TEM pictures in Fig. 2**(c-f)**, the thicknesses of SnS_2-100, SnS_2-150 and SnS_2-200 are mainly distributed at about 15–25 nm, 20 nm, and 15 nm, respectively. Obviously, with the increase of temperature, the thickness of the nanosheets tend to be thinner in the temperature range from 30 °C to 200 °C. However, the thickness will become thicker when the temperature reaches 250 °C because of the surface oxidation. When SnS_2 was subjected to thermal shock in air, the heat between the layers will dissipate slowly, causing the sublimation of upper layer and the decrease of nanosheet thickness [31–33] and Fig. 2(g) shows the diagram of SnS_2 nanosheets thickness change.

The XPS results of four samples are shown in Fig. S3 **and** Fig. 3. Fig. 3 **(a)** shows the two characteristic peaks of Sn $3d_{5/2}$ and $3d_{3/2}$ at about 486.7 and 495.2 eV. The distance was about 8.5 eV between the two peaks, which indicates the presence of Sn^{4+} [34]. The characteristic peaks of S $2p_{3/2}$ and $2p_{1/2}$ are respectively at 161.7 and 162.9 eV with a peak splitting of 1.2 eV, which are related to the S^{2-} [29]. The contents of Sn and S elements in four samples are shown in Table 1, and the ratios were 1: 1.97, 1: 1.97, 1: 1.92 and 1: 1.18, respectively. Deviations from the stoichiometric ratio also demonstrate the presence of Sv. In addition, element of O in samples is also considered, and the peaks of lattice oxygen (O_L), absorbed oxygen (O_A), and other oxygenated gas molecules such as CO_2 and H_2O (O_C) are obtained at about 531.02, 532.30 and

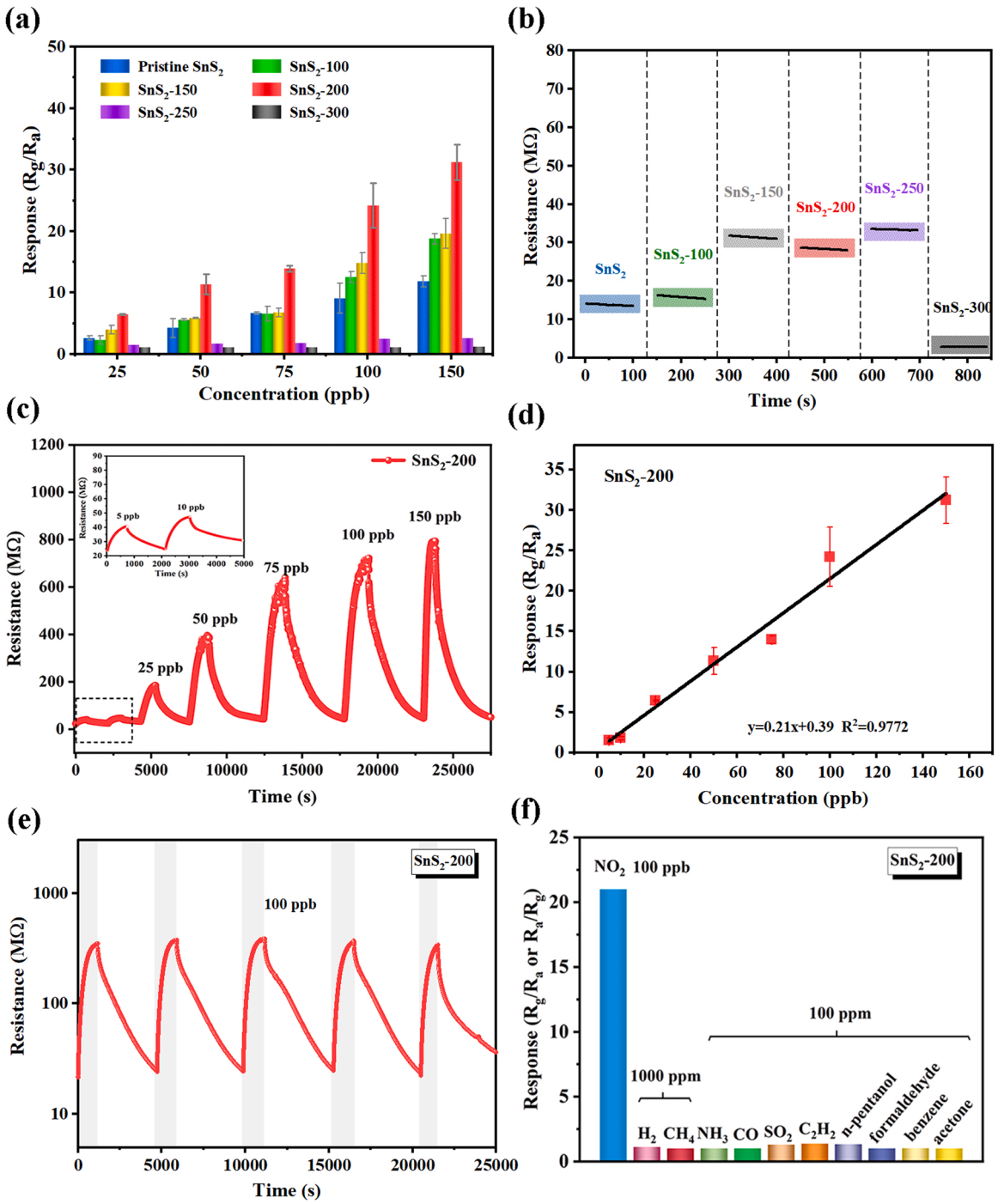

Fig. 4. (a) The responses of six sensors to different concentrations of NO_2; (b) The base resistance of five samples at RT in air; (c) The dynamic resistance curves of SnS_2-200 to 5-150 ppb NO_2 (the inset is the enlarged view to 5 and 10 ppb NO_2); (d) the linear fitting of responses; (e) the repeatability to 100 ppb NO_2; (f) the selectivity of SnS_2-200.

533.06 eV, respectively [35]. For SnS_2-300, the high content of O_L results from the fact that most of SnS_2 on the surface is oxidized to SnO_2, and the absence of O_L in other samples suggests the purity of SnS_2 materials. In fact, the presence of S_V and adsorbed oxygen both participate in gas sensing process, while S_V plays more important role in sulfide semiconductors [8,9].

3.2. The gas-sensing properties of samples

The responses of pristine SnS_2, SnS_2-100, SnS_2-150, SnS_2-200, SnS_2-250 and SnS_2-300 sensors to 25–150 ppb NO_2 are shown in Fig. 4**(a)**. SnS_2-200 displays highest sensitivity with the maximum response of 24.2 to 100 ppb NO_2. SnS_2-250 and SnS_2-300 are less sensitive to ppb-level NO_2, which is related to the partial oxidation of SnS_2 during annealing. The surface catalytic activity of SnO_2 is not as good as that of SnS_2 and SnO_2 also prevents the gas adsorption on the surface of SnS_2 [36,37]. What's more, the initial resistance values of several samples have been shown including one hundred data points in Fig. 4(b), respectively. It can be found that the resistance first increases and then decreases with the increase of annealing temperature. During low temperature annealing, there are still amino groups that remain on the surface, which acts as electron donors to improve the conductivity of

Table 2
The comparison of gas sensing properties of sensors based on SnS_2 in this work and other reported in literatures.

Materials	LOD (ppm)	Concentrations (ppm)	Response	Conditions	
				RH	
Al@SnS_2[51]	0.250	2	5.1	RT	30 %
SnO_2 nanoflowers [6]	0.320	5	9.92	Blue light	30 %
SnO_2@SnS_2[52]	–	0.2	5.30	Blue light	85 %
g-C_3N_4@SnS_2[53]	0.125	1	5.13	RT	30 %
MoS_2@SnS_2[54]	0.050	100	25.9	RT	30 %
SnS_2 nanosheets [11]	0.038	8	10.8	Green light	Dry air
ZnO@rGO[55]	0.100	10	6.77	RT	30 %
SnS_2 nanopetals (this work)	0.005	0.1	19.71	RT	60 %

SnS_2 [38]. With the increase of annealing temperature, the number of amino groups decreases leading an increase of the resistance. However, when the temperature is further increased, SnO_2 with higher conductivity will be formed. However, a small amount of SnO_2 and SnS_2 form a heterojunction, the resistance will be slightly increased, and when the content of SnO_2 is greatly increased, the resistance decreased significantly. In addition, the presence of amino groups also affects the stability of sensors. For the pristine SnS_2, three dynamic resistance curves are tested repeatedly, as shown in Fig. S4. When the sensor exposed to NO_2, the amino group will attract and rapidly aggregate NO_2 under the action of hydrogen bonds, and a high response can be obtained quickly even with a low content of S_V. However, the surface groups will be gradually consumed due to the instability, resulting in an increase in the basic resistance and a decrease in the response [39–41]. Therefore, considering the influence of various factors including content of S_V, surface groups and thickness of nanopetals, SnS_2-200 is considered to have the greatest advantages for the NO_2 gas sensing.

Fig. 4(c) shows the dynamic resistance curve of SnS_2-200 to 5-150 ppb NO_2 and the linear fitting curve between the responses and NO_2 concentrations is exhibited in Fig. 4(d). Notably, the lowest detection limit of SnS_2-200 sensor is as low as 5 ppb with a response of 1.71. Such an ultra-low detection limit of the sensor is due to the fact that the depletion layer thickness is closer to that of nanopetals and abundant S_V [42]. Besides, the repeatability of SnS_2-200 to 100 ppb NO_2 is shown in Fig. 4(e). During 5 consecutive test cycles, the dynamic resistance curve maintains good consistency indicating good repeatability of the SnS_2-200 sensor. The properties of sensors based on SnS_2 in previous work are collected and compared in Table 2, which indicated the sensor in this work has an outstanding gas sensing response and an extremely low detection limit.

The selectivity of SnS_2-200 is depicted in Fig. 4**(f)**. The responses of SnS_2-200 to interference gases such as 100 ppm NH_3, CO, SO_2, C_2H_2, n-pentanol, formaldehyde, benzene, acetone and 1000 ppm H_2 and CH_4 are much lower than that to 100 ppb NO_2. The influence of humidity on response is also explored in the RH range of 30 %– 90 % in a humidity cabinet with setting temperature of 25 °C and the result is shown in Fig. 5(a). As the humidity increases, the response value decreases due to the adsorption of water molecules, while the sensor still has enough capacity to detect 100 ppb NO_2 even at the high humidity condition. Moreover, the humidity in the indoor environment is easily controlled in a relatively stable range, so the influence of humidity can be easily controlled to a certain extent.

The sensing properties of SnS_2-200 at 50 °C, 100 °C and 150 °C are compared with that at RT in Fig. S5. It can be seen that with the increase of temperatures, the basic resistance decreased significantly and the response/recovery speeds are greatly accelerated. However, due to the faster dynamic equilibrium process of NO_2 adsorption and desorption on the surface, the responses greatly decreased [43,44]. Therefore, the SnS_2-200 sensor is more suitable for working at RT, which can not only ensure sufficient response, but also helps to prolong the lifetime of the sensor.

In addition, previous studies indicate the illumination also has varying degrees of influence on the responses and response/recovery speeds of the sensors [45,46], which is expected to be used for the improvement of response/recovery speeds. According to this, the response curves of SnS_2-200 are measured to 0.1–8 ppm NO_2 under 520 nm light that close to the edge of SnS_2 absorption band, as shown in Fig. S6**(a)**. The response is 2.30 to 100 ppb NO_2, and the response/recovery time are 179 s and 782 s in Fig. S6(b), respectively. Although the response is not enhanced under light irradiation, the speeds of response and recovery are greatly improved. Compared with response and recovery time without light (12.9 min and 33.9 min, respectively), that under light are respectively reduced by 4.3 times, and 2.6 times. I-V characteristic of SnS_2-200 has good linearity with the voltages from − 3–3 V, indicating good ohmic contact between the material and the electrode in Fig. S6(c). Compared with no illumination, SnS_2-200 performs a dramatic enhancement of conductivity under the green light. A large number of photogenerated carriers not only greatly increase the conductivity of the material, but also improves the surface gas-sensing reaction rate. Therefore, high response and fast recovery speed can be obtained at the same time by controlling the light off and on, as shown in

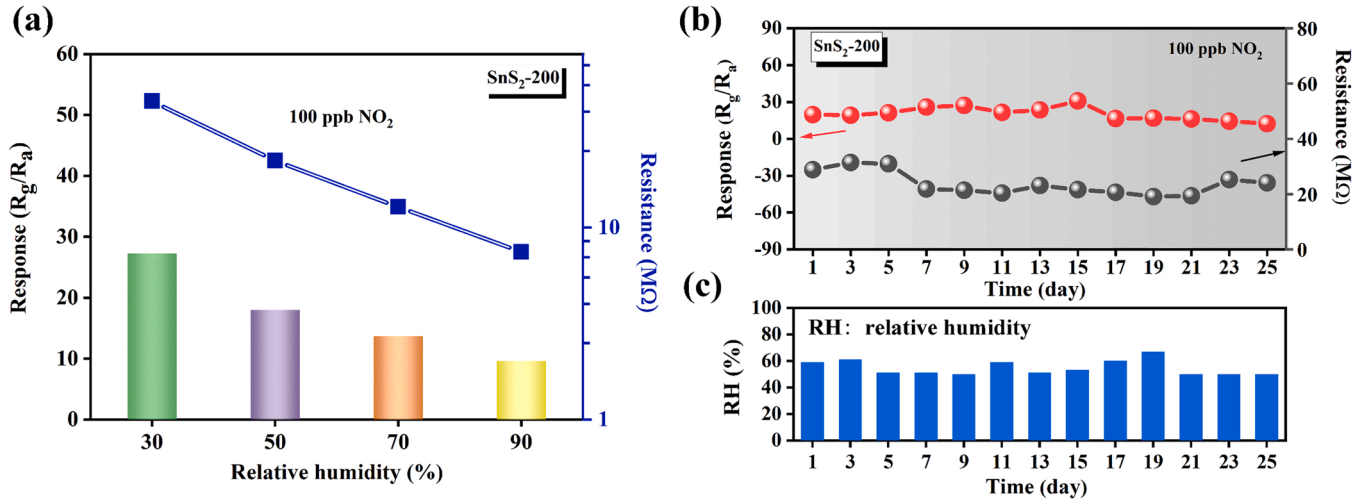

Fig. 5. (a) The influence of different humidity on the response and the initial resistance of SnS_2-200 (relative humidity is provided by the humidity cabinet with the setting temperature of 25 °C); (b-c) the stability of SnS_2-200 at RT in a month under relative humidity.

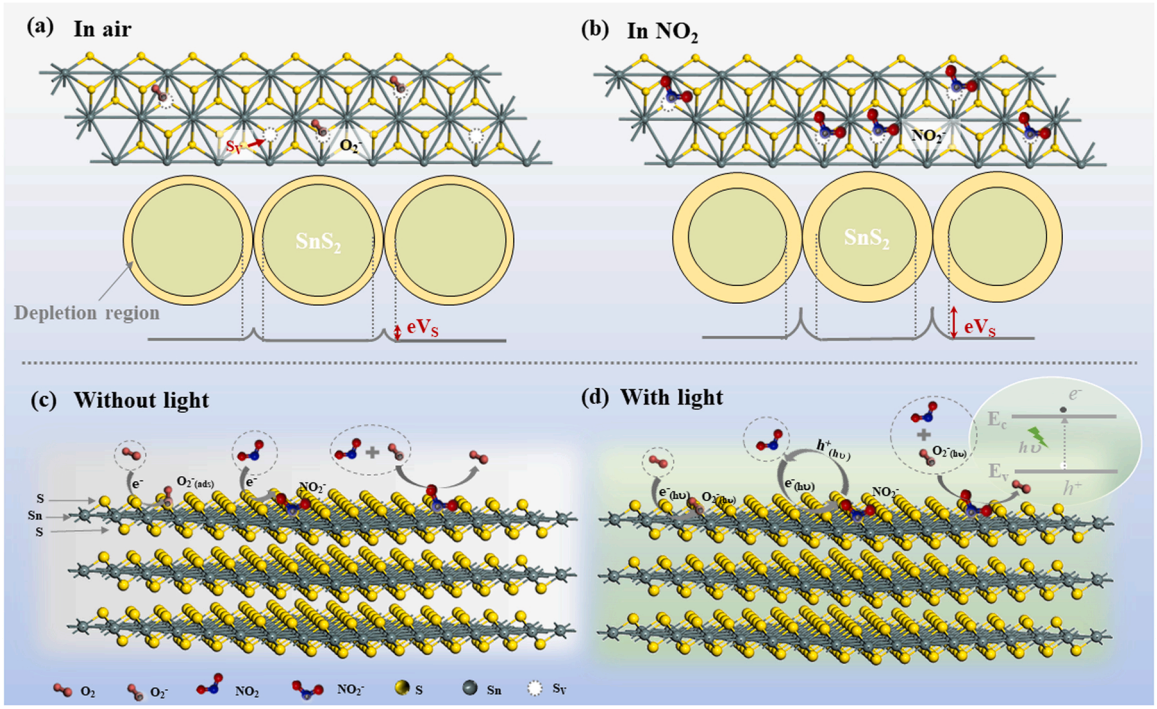

Fig. 6. The schematical illustration of gas sensing analysis: (a-b) in air and NO_2; (c-d) without and with the light.

Fig. S6(d). For the long-term stability, the responses of sensor to 100 ppb NO_2 are recorded every 2 days during a month (Fig. 5(b-c)). The base resistance of the sensor, as well as the response value, fluctuates within acceptable limits. Despite the sensor being stored for 5 months, it still exhibits consistent response and recovery characteristics (Fig. S7).

3.3. The gas sensing mechanism

The excellent sensing properties of NO_2 sensors based on SnS_2 are attributed to three aspects. On one hand, the content of S_V has a great influence on the gas sensing properties. SnS_2 crystals often exhibit the characteristics of N-type semiconductors because of the existence of trace defects especially S_V, which improves the catalytic activity of the surface of SnS_2 and becomes a reaction site during chemical adsorption. S_V not only adsorbs O_2 to produce oxygen ions (mainly O_2^- at RT [47]) which reacts with NO_2, but also induces the strong adsorption between NO_2 and SnS_2, which plays a major role in the gas-sensing process [8,9,48]. From XPS and UV–vis spectroscopy results, it can be seen that the calcination temperature will affect the content of S_V in SnS_2, resulting in different gas-sensing responses. On the other hand, the thickness of SnS_2 nanosheets can be regulated by different calcination temperatures, leading to the lower detection limit. The depletion layer through the adsorption of NO_2 molecules is close to the thickness of the nanosheets, and the resistance will have a drastic change when exposed to trace-level NO_2 [42,48]. Furthermore, NO_2 as a paramagnetic gas can easily adsorbed on the SnS_2 surface by the interface electron exchange at RT and NO_2 sensors always tend to exhibit excellent selectivity compared to other non-paramagnetic gases sensors [8].

The schematic diagrams of reactions on the SnS_2 surface are exhibited in Fig. 6. In air, O_2 will adsorb on the S_V and takes electrons from the surface of SnS_2 to form $O_{2(ads)}^-$ [49]. The resistance of SnS_2 increases due to the formed depletion layer on the surface. In the presence of NO_2 gas, NO_2 molecules will partially react with $O_{2(ads)}^-$. Most of them will interact with S_V to obtain electrons from the conduction band of SnS_2, which deepens the depletion layer width resulting in the significant increase of resistance [8]. As shown in Fig. 6(a-b), compared with the SnS_2 in air, the ions adsorbed on the surface changed to NO_2^- in NO_2 atmosphere, and the thickness of the surface depletion layer of SnS_2 grains increased due to the presence of NO_2^- and the energy band bending was deepened so that the resistance of the material increases significantly. Meanwhile, a handful of $NO_{2(ads)}^-$ will combine with the holes and change back to NO_2. Eventually, the reactions reach equilibrium, and the resistance of the material increases to a relatively stable state. The reaction equations are as follows:

$$O_{2(air)} + e^- \rightarrow O_{2(ads)}^- \quad (3)$$

$$NO_{2(ads)} + e^- \rightarrow NO_{2(ads)}^- \quad (4)$$

$$NO_{2(ads)} + O_{2(ads)}^- \rightarrow NO_{2(ads)}^- + O_{2(gas)} \quad (5)$$

$$NO_{2(ads)}^- + h^+ \rightarrow NO_{2(ads)} \quad (6)$$

Under light conditions, the reaction process can be expressed by Eqs. 7–10 [11]. A large number of photogenerated carriers improve carrier density and electron transfer speed, increasing the reaction rate with NO_2. Besides, $O_{2(h\upsilon)}^-$ adsorbed on the surface are more active than O_2^-, so the response time will be also significantly improved [18,50]. However, more $h_{(h\upsilon)}^+$ will combine with $NO_{2(ads)}^-$ to lead to the photodesorption of NO_2 molecules and reduce the sensitivity of the sensors (Eq. 10). The surface reactions without or with the light were comparatively shown in Fig. 6(c-d).

$$O_{2(air)} + e_{(h\upsilon)}^- \rightarrow O_{2(h\upsilon)}^- \quad (7)$$

$$NO_{2(ads)} + e_{(h\upsilon)}^- \rightarrow NO_{2(ads)}^- \quad (8)$$

$$NO_{2(ads)} + O_{2(h\upsilon)}^- \rightarrow NO_{2(ads)}^- + O_{2(gas)} \quad (9)$$

$$NO_{2(ads)}^- + h_{(h\upsilon)}^+ \rightarrow NO_{2(ads)} \quad (10)$$

4. Conclusions

The SnS_2 flowers with ultra-thin nanopetals were synthesized by a facile one-step solvothermal method. The sensors were annealed in the air of the muffle furnace at different temperatures and their sensing

properties to NO_2 were compared and investigated. As a result, the sensor annealed at 200 °C in the air of the muffle furnace exhibits best sensing characteristics with highest properties. The optimal annealing temperature of 200 °C can not only reduce the thickness of nanopetals, but also help to generate a higher number of S_V thus making the sensor to realize the detection of trace-level NO_2 at RT. In addition, the recovery speed can be greatly improved under the excitation of green light. The good sensing characteristics makes the sensor based on SnS_2 flowers with ultra-thin nanopetals a promising candidate for the trace-level NO_2 detection.

CRediT authorship contribution statement

Li Yueyue: Conceptualization, Investigation, Methodology, Data curation, Formal Analysis, Software, Writing – original draft, Writing – review & editing. **Dai Meng:** Formal Analysis, Visualization, Software, Writing – review & editing. **Bai Jihao:** Formal Analysis, Investigation, Methodology, Writing – review & editing. **Wang Yilin:** Methodology, Software, Writing – review & editing. **Li Yuan:** Investigation, Formal Analysis, Software. **Wang Chenchang:** Investigation, Formal Analysis, Software. **Liu Fengmin:** Conceptualization, Methodology, Formal Analysis, Supervision, Funding acquisition, Writing – review & editing. **Sun Peng:** Conceptualization, Methodology, Formal Analysis, Supervision, Funding acquisition, Writing – review & editing. **Wang Tianshuang:** Conceptualization, Methodology, Formal Analysis, Supervision, Funding acquisition, Writing – review & editing. **Geyu Lu:** Conceptualization, Supervision, Validation, Project administration, Writing – review & editing.

Declaration of Competing Interest

The authors declare that they have no known competing financial interests or personal relationships that could have appeared to influence the work reported in this paper.

Acknowledgements

This work was supported by the National Key Research and Development Program of China (No. 2021YFB3201301), National Natural Science Foundation of China (Nos. 61871198, 61831011 and 61833006), and Project on Industrial Innovation Capability of Jilin Province (No. 2020C048).

Appendix A. Supporting information

Supplementary data associated with this article can be found in the online version at doi:10.1016/j.snb.2022.132398.

References

[1] Y. Hu, et al., Relationship between indoor and outdoor NO_2: A review, Build. Environ. 180 (2020), 106909.
[2] J.M. Logue, et al., Pollutant exposures from natural gas cooking burners: a simulation-based assessment for Southern California, Environ. Health Perspect. 122 (2014) 43–50.
[3] S. Chowdhury, et al., Global and national assessment of the incidence of asthma in children and adolescents from major sources of ambient NO_2, Environ. Res. Lett. 16 (2021), 035020.
[4] P.H. Fischer, et al., Air pollution and mortality in seven million adults: the dutch environmental longitudinal study (DUELS), Environ. Health Perspect. 123 (2015) 697–704.
[5] J. Zuniga, et al., Assessment of the possible association of air pollutants PM_{10}, O_3, NO_2 with an increase in cardiovascular, respiratory, and diabetes mortality in Panama City: A 2003 to 2013 data analysis, Medicine 95 (2016), e2464.
[6] J.Q. Yang, et al., Sn doping effect on NiO hollow nanofibers based gas sensors about the humidity dependence for triethylamine detection, Sens. Actuators B Chem. 340 (2021), 129971.
[7] S.M. Majhi, et al., Recent advances in energy-saving chemiresistive gas sensors: a review, Nano Energy 79 (2021), 105369.
[8] J.Z. Ou, et al., Physisorption-based charge transfer in two-dimensional SnS2 for selective and reversible NO_2 Gas Sensing, Acs Nano 9 (2015) 10313–10323.
[9] W.-J. Yan, et al., Photo-enhanced gas sensing of SnS_2 with nanoscale defects, RSC Adv. 9 (2019) 626–635.
[10] H.B. Mabiala-Poaty, et al., First-principles studies of SnS_2, MoS_2 and WS_2 stacked van der Waals hetero-multilayers, Comput. Condens. Matter 16 (2018), e00303.
[11] D. Gu, et al., Visible-light activated room temperature NO_2 sensing of SnS_2 nanosheets based chemiresistive sensors, Sens. Actuators B Chem. 305 (2020), 127455.
[12] W. Hu, et al., Enhancement in photoelectrochemical performance of optimized amorphous SnS_2 thin film fabricated through atomic layer deposition, Nanomater. -Basel 9 (2019) 1083.
[13] M. Tonezzer, et al., Comparative gas-sensing performance of 1D and 2D ZnO nanostructures, Sens. Actuators B Chem. 220 (2015) 1152–1160.
[14] M. Tonezzer, et al., H_2 sensing properties of two-dimensional zinc oxide nanostructures, Talanta 122 (2014) 201–208.
[15] J.X. Xu, et al., SnS_2/Si vertical heterostructure for high-performance photodetection with large photocurrent and fast speed, Appl. Surf. Sci. 506 (2020), 144671.
[16] S. Palleschi, et al., On the role of nano-confined water at the 2D/SiO_2 interface in layer number engineering of exfoliated MoS_2 via thermal annealing, 2d Mater. 7 (2020).
[17] J. Feng, et al., Microwave-assistant synthesis of Au/SnS_2 nanoflowers as improved visible-light responsive photocatalysts, Mater. Lett. 236 (2019) 534–537.
[18] H. Wang, et al., Visible light activated excellent NO_2 sensing based on 2D/2D ZnO/g-C_3N_4 heterojunction composites, Sens. Actuators B Chem. 304 (2020), 127287.
[19] T. Duangchuen, et al., Effect of SnS_2 concentrations on electrochemical properties of SnS2/RGO nanocomposites synthesized by a one-pot hydrothermal method, Appl. Surf. Sci. 487 (2019) 634–646.
[20] H. Cui, et al., Adsorption and sensing of CO and C_2H_2 by S-defected SnS_2 monolayer for DGA in transformer oil: a DFT study, Mater. Chem. Phys. 249 (2020), 123006.
[21] G. Li, et al., Band gap narrowing of SnS_2 superstructures with improved hydrogen production, J. Mater. Chem. A 4 (2016) 209–216.
[22] L. Dashairya, et al., SnS_2/RGO based nanocomposite for efficient photocatalytic degradation of toxic industrial dyes under visible-light irradiation, J. Alloy. Compd. 774 (2019) 625–636.
[23] Z. Wu, et al., SnS_2 nanosheet-based microstructures with high adsorption capabilities and visible light photocatalytic activities, RSC Adv. 5 (2015) 24640–24648.
[24] P. Saha, et al., Reduced graphene oxide modified melamine formaldehyde (rGO@MF) superhydrophobic sponge for efficient oil–water separation, J. Porous Mater. 25 (2018) 1475–1488.
[25] H.F. Xie, et al., Multi-wall carbon nanotube gas sensors modified with amino-group to detect low concentration of formaldehyde, Sens. Actuators B Chem. 168 (2012) 34–38.
[26] L.T.M. Hoa, Surface functionalisation of multi-walled carbon nanotubes with tris (2-aminoethyl)amine and their characterisation, Adv. Nat. Sci.: Nanosci. Nanotechnol. 12 (2021).
[27] S. Polivtseva, et al., Thermoanalytical study of precursors for tin sulfide thin films deposited by chemical spray pyrolysis, J. Therm. Anal. Calor. 121 (2015) 177–185.
[28] H. Su, et al., Preparation and morphology control of rod-like nanocrystalline tin sulfides via a simple ethanol thermal route, J. Solid State Chem. 161 (2001) 190–196.
[29] Z. Khan, et al., Three-dimensional SnS_2 nanopetals for hybrid sodium-air batteries, Electrochim. Acta 257 (2017) 328–334.
[30] G.W. Li, et al., Controlled self-assembly of PbS nanoparticles into macrostar-like hierarchical structures, Mater. Res. Bull. 46 (2011) 1072–1079.
[31] M. Yamamoto, et al., Anisotropic Etching of Atomically Thin MoS_2, J. Phys. Chem. C. 117 (2013) 25643–25649.
[32] A. Castellanos-Gomez, et al., Laser-thinning of MoS_2: on demand generation of a single-layer semiconductor, Nano Lett. 12 (2012) 3187–3192.
[33] J. Wu, et al., Layer thinning and etching of mechanically exfoliated MoS_2 nanosheets by thermal annealing in air, Small 9 (2013) 3314–3319.
[34] W.E. Morgan, J.R. Van Wazer, Binding energy shifts in the x-ray photoelectron spectra of a series of related Group IVa compounds, J. Phys. Chem. 77 (1973) 964–969.
[35] K. Sutthiumporn, et al., Promotional effect of alkaline earth over Ni–La_2O_3 catalyst for CO_2 reforming of CH_4: Role of surface oxygen species on H_2 production and carbon suppression, Int. J. Hydrog. Energy 36 (2011) 14435–14446.
[36] A. Gaiardo, et al., Metal sulfides as sensing materials for chemoresistive gas sensors, Sensors-Basel 16 (2016).
[37] X.D. Cui, et al., Hierarchical SnO_2@SnS_2 counter electrodes for remarkable high-efficiency dye-sensitized solar cells, Electrochim. Acta 186 (2015) 125–132.
[38] W.P. Hu, et al., The gas sensitivity of Langmuir-Blodgett films of a new asymmetrically substituted phthalocyanine, Sens. Actuators B Chem. 56 (1999) 228–233.
[39] T. Russ, et al., Operando investigation of the aging mechanism of lead sulfide colloidal quantum dots in an oxidizing background, J. Phys. Chem. C. 125 (2021) 19847–19857.
[40] Y.J. Wang, et al., An ultrafast responsive NO_2 gas sensor based on a hydrogen-bonded organic framework material, Chem. Commun. 56 (2020) 703–706.
[41] A. Gamonal, et al., Divergent adsorption-dependent luminescence of amino-functionalized lanthanide metal-organic frameworks for highly sensitive NO_2 sensors, J. Phys. Chem. Lett. 11 (2020) 3362–3368.
[42] W. Zeng, et al., Effects of different petal thickness on gas sensing properties of flower-like WO_3 center dot H_2O hierarchical architectures, Appl. Surf. Sci. 347 (2015) 73–78.

[43] M. Shafiei, et al., Low-operating temperature NO_2 gas sensors based on hybrid two-dimensional SnS2-reduced graphene oxide, Appl. Surf. Sci. 462 (2018) 330–336.
[44] D. Liu, et al., Nanoplates-assembled SnS2 nanoflowers for ultrasensitive ppb-level NO_2 detection, Sens. Actuators B Chem. 273 (2018) 473–479.
[45] A. Chen, et al., 2D hybrid nanomaterials for selective detection of NO_2 and SO_2 using "Light On and Off" strategy, ACS Appl. Mater. Interfaces 9 (2017) 37191–37200.
[46] Y. Huang, et al., SnS_2 quantum dot-based optoelectronic flexible sensors for ultrasensitive detection of NO_2 down to 1 ppb, ACS Appl. Mater. Interfaces 12 (2020) 25178–25188.
[47] H.T. Wang, et al., UV-activated ultrasensitive and fast reversible ppb NO_2 sensing based on ZnO nanorod modified by constructing interfacial electric field with In_2O_3 nanoparticles, Sens. Actuators B Chem. 305 (2020), 127498.
[48] J.J. Pyeon, et al., Highly sensitive flexible NO_2 sensor composed of vertically aligned 2D SnS_2 operating at room temperature, J. Mater. Chem. C. 8 (2020) 11874–11881.
[49] Y.F. Huang, et al., SnS_2 quantum dot-based optoelectronic flexible sensors for ultrasensitive detection of NO_2 down to 1 ppb, ACS Appl. Mater. Interfaces 12 (2020) 25178–25188.
[50] D. Haridas, et al., Enhanced room temperature response of SnO_2 thin film sensor loaded with Pt catalyst clusters under UV radiation for LPG, Sens. Actuators B Chem. 153 (2011) 152–157.
[51] Q. Sun, et al., Synergically engineering defect and interlayer in SnS_2 for enhanced room-temperature NO_2 sensing, J. Hazard. Mater. 421 (2021), 126816.
[52] D. Liu, et al., Visible light assisted room-temperature NO_2 gas sensor based on hollow SnO_2@SnS_2 nanostructures, Sens. Actuators B Chem. 324 (2020), 128754.
[53] Q. Sun, et al., 2D/2D heterojunction of g-C_3N_4/SnS_2: room-temperature sensing material for ultrasensitive and rapid-recoverable NO_2 detection, Nanotechnology 31 (2020), 425502.
[54] L. Liu, et al., Edge-exposed MoS_2 nanospheres assembled with SnS_2 nanosheet to boost NO_2 gas sensing at room temperature, J. Hazard. Mater. 393 (2020), 122325.
[55] R. Gao, et al., The controllable assembly of the heterojunction interface of the ZnO@rGO for enhancing the sensing performance of NO_2 at room temperature and sensing mechanism, Sens. Actuators B Chem. 342 (2021), 130073.

Li Yueyue received the B.Eng. degree in department of electronic science and technology in 2019. She is currently studying for her Ph.D. degree in College of Electronic Science and Engineering, Jilin University, China.

Dai Meng received the B.S. degree in department of micro-electronics in 2018. She received her M.E. Sci. degree in College of Electronic Science and Engineering in 2021, Jilin University, China.

Bai Jihao received the B.S. degree in department of micro-electronics in 2018. He is currently studying for his Ph.D. degree in College of Electronic Science and Engineering, Jilin University, China.

Wang Yilin received the B.Eng. degree in department of electronic science and technology in 2020. She is currently studying for her M.E. Sci. degree in College of Electronic Science and Engineering, Jilin University, China.

Li yuan received the B.Eng. degree in department of electronic science and technology in 2019. He is currently studying for her M.E. Sci. degree in College of Electronic Science and Engineering, Jilin University, China.

Wang Chenchang received the B.S. degree in department of micro-electronics in 2019. She is currently studying for her M.E. Sci. degree in College of Electronic Science and Engineering, Jilin University, China.

Liu Fengmin received the B.S. degree in department of electronic science and technology in 2000. She received her Ph.D degree in College of Electronic Science and Engineering at Jilin University in 2005. Now she is a professor in Jilin University, China. Her current research is preparation and application of semiconductor oxide, especial in gas sensor and solar cell.

Sun Peng received his Ph.D. degree from the Electronics Science and Engineering department, Jilin University, China in 2014. Now, he is engaged in the synthesis and characterization of the semiconducting functional materials and gas sensors.

Wang Tianshuang received his Ph.D. degree from Jilin University in 2020. He is now a Postdoctoral Fellow at State Key Laboratory of Inorganic Synthesis and Preparative Chemistry, Jilin University. His research focuses on the development of porous structure metal oxide and multi-functional zeolite catalysts for chemical sensor application.

Lu Geyu received the B.Sci. degree in electronic sciences in 1985 and the M.S. degree in 1988 from Jilin University in China and the Dr. Eng. degree in 1998 from Kyushu University in Japan. Now he is a professor of Jilin University, China. His current research interests include the development of chemical sensors and the application of the function materials.